nature physics

ARTICLES

https://doi.org/10.1038/s41567-021-01493-9

Check for updates

# Diffusive topological transport in spatiotemporal thermal lattices

Guoqiang Xu[1], Yihao Yang[2,3,4], Xue Zhou[5], Hongsheng Chen[2,3,4], Andrea Alù[6,7] and Cheng-Wei Qiu[1]✉

**Topological phases have been studied in photonic, acoustic and phononic metamaterials, promising a range of applications. Such topological modes usually stem from collective resonant effects in periodic lattices. One may, therefore, expect similar features to be forbidden for thermal diffusion that is purely dissipative and mostly incoherent, prohibiting collective resonances. Here we report the discovery of diffusion-based topological states supported by spatiotemporally modulated advections stacked over a fluidic surface. This arrangement imitates a periodic propagating potential in an effective thermal lattice. We observe edge states in topologically non-trivial and bulk states in topologically trivial lattices. Interface states form at boundaries between these two types of lattice, manifesting inhomogeneous thermal properties on the fluidic surface. Our findings establish a framework for topological diffusion and thermal edge or bulk states, and it may allow a distinct mechanism for the flexible manipulation of diffusive phenomena for robust heat and mass transfer.**

Topological insulating phases[1–5] have been unveiling a variety of new wave phenomena in metamaterials. A particularly interesting class of topological phenomena arises in open systems[6–9], enabling novel phenomena across a variety of fields[10–13], such as anomalous edge states[14], mode switching[15,16], unidirectional wave propagation[17,18], single-mode laser[19,20], pump-dependent lasing[21–25] and so on. Two main recipes have been proposed to realize these classes of non-Hermitian topological responses. The first option is to drive the topological responses by magneto-optic effects[26] or tailored lattice coupling[27] in cooperation with the introduced non-Hermitian elements; the second is to induce non-trivial topological phases by pumping non-Hermitian elements like gain and loss[28–36] into otherwise Hermitian systems.

Recently, the Hamiltonian associated with classical thermal exchange was discovered to follow a skew-Hermitian relation[37], which may offer a hint to realize a topological insulating phase for thermal diffusion. On the other hand, the absence of a periodic potential and dynamic coherence for thermal transport fundamentally hinders this pathway. To synthesize a topological insulating phase in purely dissipative diffusion mechanism, it is of utmost importance to imitate the periodic potential and coherent interference in thermal transport, such that Bloch theory could be revived and diffusive topological transport could be thereby expected as the photonic and acoustic counterparts[18–28].

Here we resort to judicious time-modulated Hermiticity features in both space and time to introduce an advective paradigm for the demonstration of thermal topological transport in periodically stacked fluid surfaces. We incorporate spatiotemporally modulated advections to enable an additional real dimension to thermal diffusion, whereas alternating advection arrangements offer imitated coherences and periodic potentials. Depending on the advective configuration, the effective bandgap can be either topologically non-trivial or trivial. We experimentally discover thermal topological modes with edge and interface states as well as conventional bulk states, manifested as stationary and deviated temperature distributions, respectively. The findings provide a feasible way of creating an effective periodic lattice on an advective fluidic surface, unlocking more opportunities and applications for topological thermal diffusion. Our proposed recipe for diffusive topological modes can further enlighten the manipulation of general diffusive fields[38–42].

We consider a planar fluid surface possessing periodic advections in a virtual space $(x_p, y_p, z)$ (Fig. 1a) to demonstrate non-Hermitian topological modes for thermal diffusion. Owing to the dissipative nature of thermal diffusion, non-Hermiticity inherently exists in the proposed system. To create an effective coherent resonance for thermal fields over the fluidic surface, we apply spatiotemporal modulation onto the corresponding advective regions[43] marked by specific colours (Fig. 1a). These advective blocks could be regarded as four modulated units, forming one effective lattice. The four-unit lattice is used to form a pair of effective dimers and a four-band system by effective decoupling between the units with the imposed advections. Such implementation could reveal multifarious band properties, topological transitions and midgap edge states for a wide range of parameters, as well as simplify practical advective arrangements, in contrast to lattices with two or three units[28–34]. Further periodic configuration of multiple effective lattices can yield an effective one-dimensional chain that can be induced on the fluidic surface. Here the heat transfer process between two neighbouring super-cells $n$ and $(n+1)$ via their joint interface in the virtual space $(x_p, y_p, z)$ can be written as

$$\rho c\frac{\partial T_n}{\partial t} = \kappa\frac{\partial^2 T_n}{\partial x_p^2} \pm \rho c v_n\frac{\partial T_n}{\partial x_p} + \frac{h_n}{a_n}\left(T_{n+1} - T_n\right). \quad (1)$$

[1]Department of Electrical and Computer Engineering, National University of Singapore, Kent Ridge, Singapore. [2]Interdisciplinary Center for Quantum Information, State Key Laboratory of Modern Optical Instrumentation, College of Information Science and Electronic Engineering, Zhejiang University, Hangzhou, China. [3]ZJU-Hangzhou Global Science and Technology Innovation Center, Key Laboratory of Advanced Micro/Nano Electronic Devices and Smart Systems of Zhejiang, Zhejiang University, Hangzhou, China. [4]International Joint Innovation Center, ZJU-UIUC Institute, The Electromagnetics Academy at Zhejiang University, Zhejiang University, Haining, China. [5]School of Computer Science and Information Engineering, Chongqing Technology and Business University, Chongqing, China. [6]Photonics Initiative, Advanced Science Research Center, City University of New York, New York, NY, USA. [7]Physics Program, Graduate Center of the City University of New York, New York, NY, USA. ✉e-mail: chengwei.qiu@nus.edu.sg

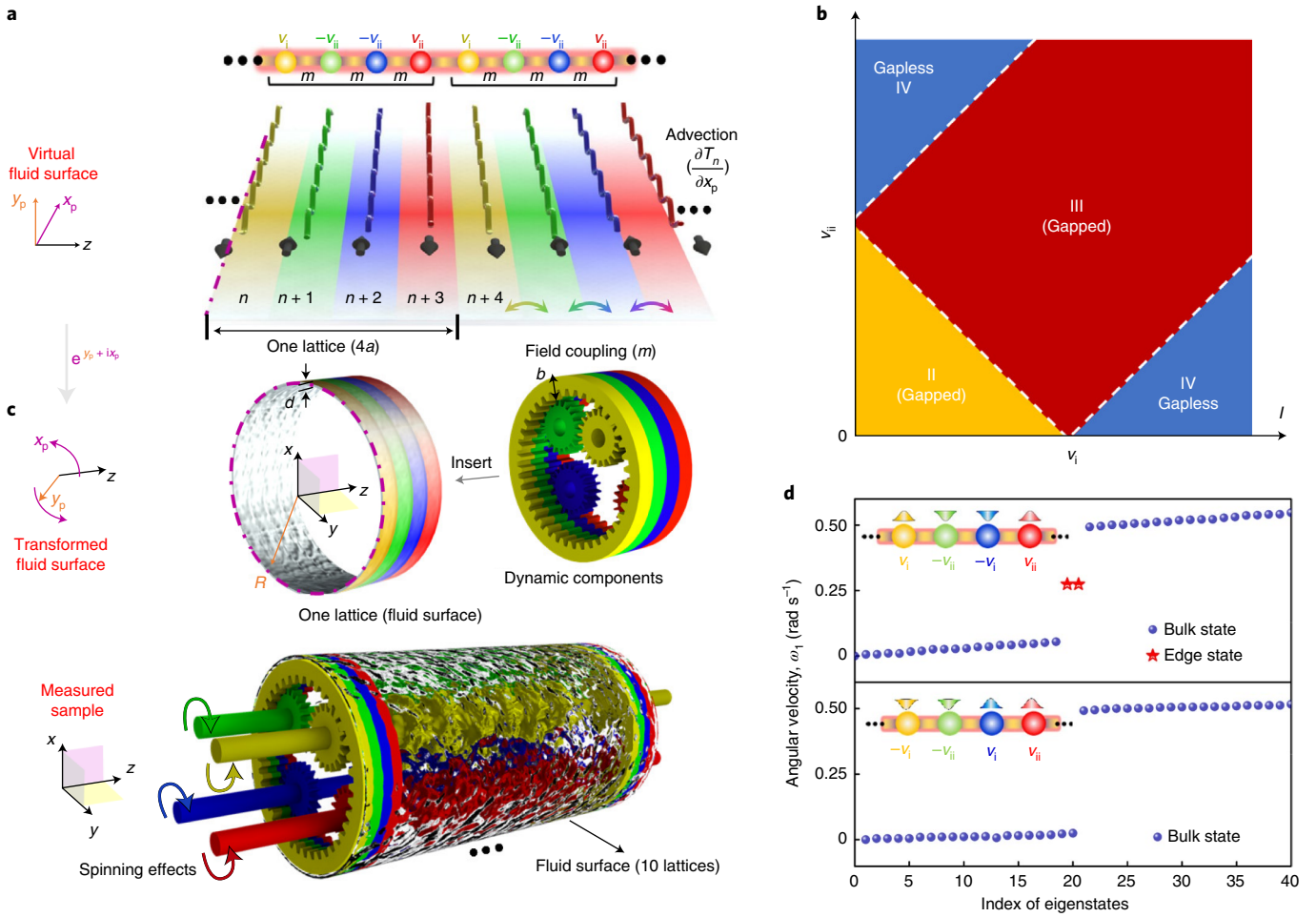


**Fig. 1 | Topological transport in thermal diffusion. a**, Schematic for realizing the topology in thermal diffusion by introducing periodic advections onto a planar fluid surface (coloured curves) in a virtual space ($x_p$, $y_p$, $z$). These periodic advections independently propagate along the $x_p$ direction and are arranged along the $z$ direction, thus contributing to the effective 'lattice' with four units marked by $n$–$(n+3)$. The lattice constant is $4a$, whereas the field coupling between two adjacent units is $m = \frac{h}{\rho c b} = \frac{\kappa}{\rho c b d}$. **b**, Phase diagram by modulating advections ($v_i$/$v_{ii}$). Among them, Phase I exists only when $v_i = 0$ or $v_{ii} = 0$; Phases II and III are gapped, whereas Phase IV is gapless. **c**, Practical model for implementations in a transformed space ($x$, $y$, $z$). It can be created via a conformal mapping with the model in the schematic, where the azimuthal and radial directions in **c** correspond to $x_p$ and $y_p$ in **a**, respectively. The purple dash-dot lines in **a** and **c** indicate their counterpart boundaries of a specific unit. Each effective lattice consists of four units on the fluid surface. They are modulated by corresponding dynamic components with consistent colours inserted under the fluid surface. The entire thermal process is modulated by ten effective lattices (bottom inset). **d**, Angular velocity (eigenfrequencies) sorted in a gapped phase as a function of $v_i = m/k$ and $v_{ii} = 2m/k$. The top and bottom insets indicate non-trivial and trivial lattices, respectively.

In equation (1), $\rho$, $c$ and $\kappa$ denote the density, specific heat and thermal conductivity of the planar fluid surface, respectively; $T_n$ is the temperature of a specific unit of one lattice (Fig. 1a), where subscript $n$ indicates the unit index counting from 1. Further, $a_n$ and $h_n$ are the width and convective heat transfer coefficient of each unit. Equation (1) is the general thermal energy equation for describing heat transfer and exchange between any two neighbouring units with a joint interface. It consists of three terms: a conductive component ($\kappa \frac{\partial^2 T_n}{\partial x_p^2}$), a convective component ($\pm \rho c v_n \frac{\partial T_n}{\partial x_p}$) and a heat exchange term via their joint interface $\frac{h_n}{a_n}(T_{n+1} - T_n)$ derived from Newton's law of cooling. It implies that heat exchange via the interface is proportional to their difference in temperatures. Hence, only temperature is involved here to describe the heat exchange between the two neighbouring layers $n$ and $(n+1)$ via their joint interface. It is worth noting that the exchange between layers $(n-1)$ and $n$ should be involved when we simultaneously take the three units $(n-1)$, $n$ and $(n+1)$—possessing two joint interfaces—as an entirety instead of the two units in equation (1). In that case, the total exchange via the two interfaces between units $(n-1, n)$ and $(n, n+1)$ becomes $\frac{h_n}{a_n}(T_{n+1} + T_{n-1} - 2T_n)$, which is the superposition of the two exchanges $\frac{h_n}{a_n}(T_{n+1} - T_n)$ and $\frac{h_n}{a_n}(T_n - T_{n-1})$ at the corresponding interfaces. This is equivalent to equation (1) since heat exchanges via each joint interface between any two neighbouring layers are the core of thermal coupling and they should be counted only one time in the effective lattice. For simplification, we adopt the same width for each unit, thus leading to an effective lattice constant of $4a$. We further assign a series of spatiotemporal advections ($v_i, -v_{ii}, -v_i, v_{ii}$) to each unit advection ($v_n, v_{n+1}, v_{n+2}, v_{n+3}$) of one lattice to create an effective 'oscillation' in such diffusive systems, that is, $\pm \rho c v_n \frac{\partial T_n}{\partial x_p}$ in equation (1). Here we make $v_i \geq 0$ and $v_{ii} \geq 0$ to indicate the scalar amplitudes of the imposed advective velocities on each unit, whereas '±' indicates the advective direction in each unit. That is, $\pm v_{i/ii}$ denotes the imposed advections

propagating along opposite directions with amplitudes $v_{i/ii}$. Owing to the spatiotemporal properties, these advective velocities imitate the periodic potential fields, yielding $v_n = v_{n+4}$ between two adjacent lattices along the $z$ direction (Supplementary Equation (2)). On the interaction of imposed advections and conductions, their thermal exchange $\frac{h_n}{a_n}(T_{n+1} - T_n)$ effectively provides the coupling within two neighbouring units via the joint interface. Under the hypothesis of small fluid thermal conductivity $\kappa$, the first-order wave-like solution $T_n = Ae^{i(k_n x_p - \omega_n t)}$ hints at the possibility of switching equation (1) to a similar form of the Schrödinger equation, where $k_n = \frac{2\pi}{L_n} = R_n^{-1}$ and $\omega_n = -i\frac{2\kappa k_n}{\rho c} - k_n v_n$ denote the effective wavenumbers and angular frequencies of the units for each lattice, respectively. The phase diagram for the effective band structure under specific advective configurations is presented in Fig. 1b, indicating four insulating Phases I–IV (Supplementary Note 2). To realize such an effective lattice in an available thermal system, we need to mimic the oscillations and periodic propagations with the imposed advection in a finite system. We adopt a strategy by connecting the two terminals along the $x_p$ direction (Fig. 1a), thus forming an annular fluid surface in the transformed space $(x, y, z)$. The $z$ direction is unchanged in this process. Such a transition (Fig. 1c) follows a general conformal mapping (Methods). The thicknesses of the advective components and annular fluid surface in the transformed space are $b$ and $d$, respectively. Owing to the same radii of each unit, the effective wavenumbers are the same for the entire system, that is, $k_n = k = R^{-1}$. The changing angular velocity corresponds to a real angular frequency $(\omega_n)$ in the actual thermal system. Based on the Bloch theorem and the imposed periodic potential (velocity) field along the $z$ direction, the effective Hamiltonian can be expressed as

$$H = i\begin{bmatrix} ikv_i & \frac{h}{\rho cb} & 0 & \frac{h}{\rho cb}e^{ik_t 4a} \\ \frac{h}{\rho cb} & -ikv_{ii} & \frac{h}{\rho cb} & 0 \\ 0 & \frac{h}{\rho cb} & -ikv_i & \frac{h}{\rho cb} \\ \frac{h}{\rho cb}e^{-ik_t 4a} & 0 & \frac{h}{\rho cb} & ikv_{ii} \end{bmatrix} - i\left(\frac{\kappa}{\rho c}k^2 + \frac{h}{\rho cb}\right) I_{4\times 4}. \quad (2)$$

where $k_t$ denotes the effective Bloch wavenumber (Supplementary Note 1), and $I$ is the indentity matrix. The Bloch theorem is applied along the $z$ direction, that is, the direction of the one-dimensional lattice arrangement. Here $D = \frac{\kappa}{\rho c}$ denotes the diffusivity, whereas we further assume $m = \frac{h}{\rho cb} = \frac{\kappa}{\rho cbd}$ for simplification under the hypothesis of small fluid surface thickness $d$ (Fig. 1c). It is worth noting that equation (2) is named as the effective Hamiltonian, since it is obtained by solving the eigenvalue problem with the effective oscillatory parameters of wavenumbers $k_n$ and angular frequencies $\omega_n$, which do not naturally exist in thermal diffusion. The mathematical presence of 'i' in the entire Hamiltonian (equation (2)) indicates that the decoupled form of the matrix of heat exchanges (equation (2)) follows the skew Hermitian, which is in sharp contrast to the coupling terms of photonic/acoustic Hamiltonians also with a four-unit lattice[28–34]. Thus, the imposed advections act as a Hermitian modulation in this diffusion scenario, and it is essentially equivalent to the non-Hermitian role played by gain and loss in the photonic counterpart[28–34]. Then, we can define the eigenvalues for the periodic lattice as

$$\begin{aligned} E_\pm &= -i\left(Dk^2 + m\right) \pm \tfrac{\sqrt{2}}{2}\sqrt{p \pm \sqrt{p^2 - q^2 - l^2}}. \\ p &= (kv_i)^2 + (kv_{ii})^2 - 4m^2, q = 2(kv_i)(kv_i), \\ s &= m^2\left(1 + e^{ik_t a}\right), l = 4m^2 \sin\left(\tfrac{k_t a}{2}\right). \end{aligned} \quad (3)$$

This system can support topological modes, since equation (2) obeys pseudo-anti-Hermiticity, that is, $H = -\eta H^\dagger \eta$, where $\eta = \mathrm{diag}(1, -1, 1, -1)$. Considering one four-unit lattice, two types of advective coupling can be expected in equation (3) with imposed advections, thus leading to effective couplings $\sqrt{\left(\frac{h}{\rho cb}\right)^2 - (kv_n \pm kv_{n+1})^2}$ between any two adjacent units. These advective couplings within the four-unit lattice support an effective bandgap $\Delta = \sqrt{p - \sqrt{p^2 - q^2}}$ and the four insulating phases shown in Fig. 1b. Here we focus on the response in gapped Phase III with $p - q > 0$ and $p < -q$. In this phase, the integer winding number is non-zero or zero when the advective arrangement is $(v_i, -v_{ii}, -v_i, v_{ii})$ or $(-v_i, -v_{ii}, v_i, v_{ii})$. The other insulating phases and corresponding properties are discussed in Supplementary Note 2.

Non-zero and zero winding numbers correspond to the presence or absence of edge states at the boundaries, respectively. To verify their presence, we consider 40 units forming 10 effective lattices in the schematic shown in Fig. 1c (lower inset) and Extended Data Fig. 1, creating a finite fluidic system. The inherent conduction between each pair of adjacent lattices acts as the hopping term to generate the underlying edge and bulk states. When we consider the advective arrangement $(v_i, -v_{ii}, -v_i, v_{ii})$ for each lattice in the selected phase, the sorted angular velocities (eigenfrequencies) indicate the emergence of a pair of topological edge states within the bandgap (Fig. 1d, top inset). If the advective arrangement becomes $(-v_i, -v_{ii}, v_i, v_{ii})$ in the same phase, only the bulk state emerges (Fig. 1d, bottom inset). The thermal distribution of the edge and bulk states in the selected phase is illustrated in Fig. 2. The captured temperature profiles at specific moments of the non-trivial lattice scheme are presented in Fig. 2a,c. The thermal behaviours are robust, with stationary temperature profiles (Fig. 2c, right) during the entire thermal process, whereas some deviations relative to initial locations can be observed at the two boundaries of the system. By further tracing the experimental azimuths and spatial locations of the maximum temperature $(T_{max})$ of each unit on the fluidic surface, we find that they correspond to the first and last lattices at the two system boundaries, respectively, and slightly move to the two sides with respect to their initial azimuths (Fig. 2a) and spatial locations (Fig. 2c), revealing the non-zero winding number $(\pm 1)$ (Supplementary Note 2). The spatial information of $T_{max}$ of the other units remains almost unchanged (Fig. 2a,c). Then, we study the state intensities of each unit, which could be described as the effective thermal resistance in analogy to topological electric circuits[35] along the $z$ direction between two adjacent units and in the $x$–$y$ plane (azimuth direction) within one unit, that is, $R_{\mathrm{eff},z} = \frac{T_{n+1,z} - T_{n,z}}{P} = \frac{\sum(\psi_{n+1} - \psi_n)}{E_\pm}$ and $R_{\mathrm{eff},xy} = \frac{\Delta T_{n+1,xy}}{P}$, respectively, where $T_{n+1,z}$ and $T_{n,z}$ are the temperature components along the $z$ direction of the adjacent lattices and $\Delta T_{n+1,xy}$ is the temperature-difference component between the highest and lowest temperatures in the $x$–$y$ plane of a specific unit. $P$ denotes the power of corresponding area. Since the eigenvalue reveals the energy per unit of time corresponding to the effective heat flux along the direction of lattice arrangements, each pole of $R_{\mathrm{eff},z}$ and $R_{\mathrm{eff},xy}$ can be used to indicate the corresponding modes on the fluidic surface. Thus, the larger $R_{\mathrm{eff},z}$ and smaller $R_{\mathrm{eff},xy}$ at the system boundaries compared with the other regions (Fig. 2e,g) hint at the existence of edge states (deviations observed in Fig. 2a,c), which suppress and contribute to the heat-flux propagation towards the corresponding directions, respectively. It is worth noting that stationary thermal distribution can be observed over the entire system, owing to the thermal equilibrium under such advective configurations. The smaller $R_{\mathrm{eff},z}$/larger $R_{\mathrm{eff},xy}$ (not at the boundaries) lead to expedited/tough heat transfer towards these directions.

In contrast, the thermal features of the scheme with trivial lattices (Fig. 1d, bottom inset) are presented in Fig. 2b,d,f,h.

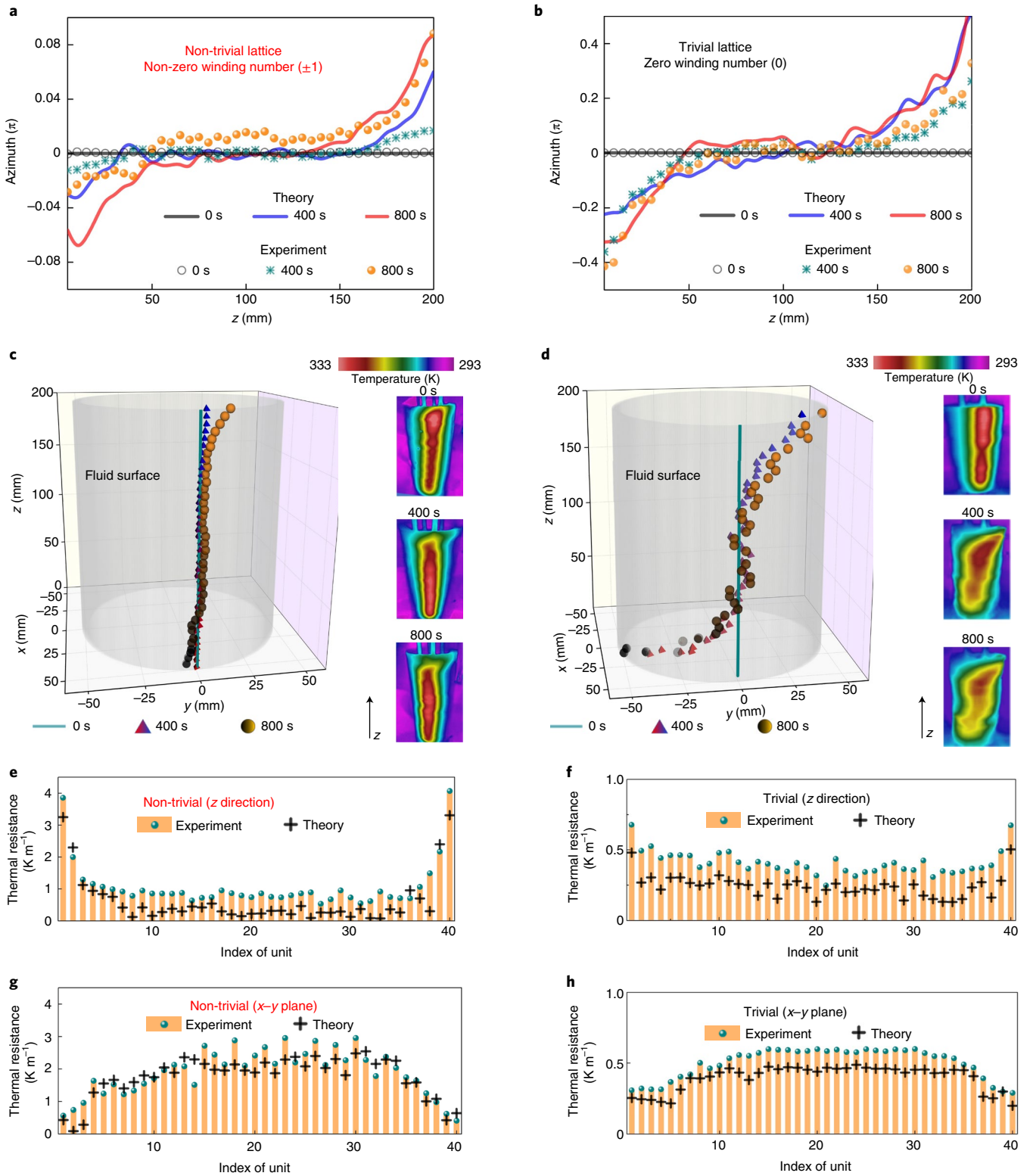


**Fig. 2 | Measured results for topologically non-trivial and trivial responses in the gapped phase. a**,**b**, Azimuths of $T_{max}$ for each unit on the fluid surface at specific moments for the non-trivial (**a**) and trivial (**b**) lattice. **c**,**d**, Visualizations of experimental $T_{max}$ locations (left) and thermal images (right) with respect to **a** (**c**) and **b** (**d**). The background colours on the projective planes correspond to the coordinates shown in Fig. 1c. The temperature profile on the fluid surface is effectively confined along the *x* and *y* directions in the non-trivial lattice, but it significantly expands along the *x* and *y* directions in the trivial lattice. These results agree well with the azimuths in **a** and **b**. The colour bars in **c** and **d** indicate the temperature ranges of the IR images. **e**,**f**, Sums of the amplitudes of the effective thermal resistance along the *z* direction for the system with the lattices in **c** (**e**) and **d** (**f**). **g**,**h**, Effective thermal resistances in the *x*–*y* plane for the two lattices in **c** (**g**) and **d** (**h**). In **e**–**h**, the orange columns with green dots denote the experimental values and '+' denotes the theoretical values of the effective thermal resistances of each unit.

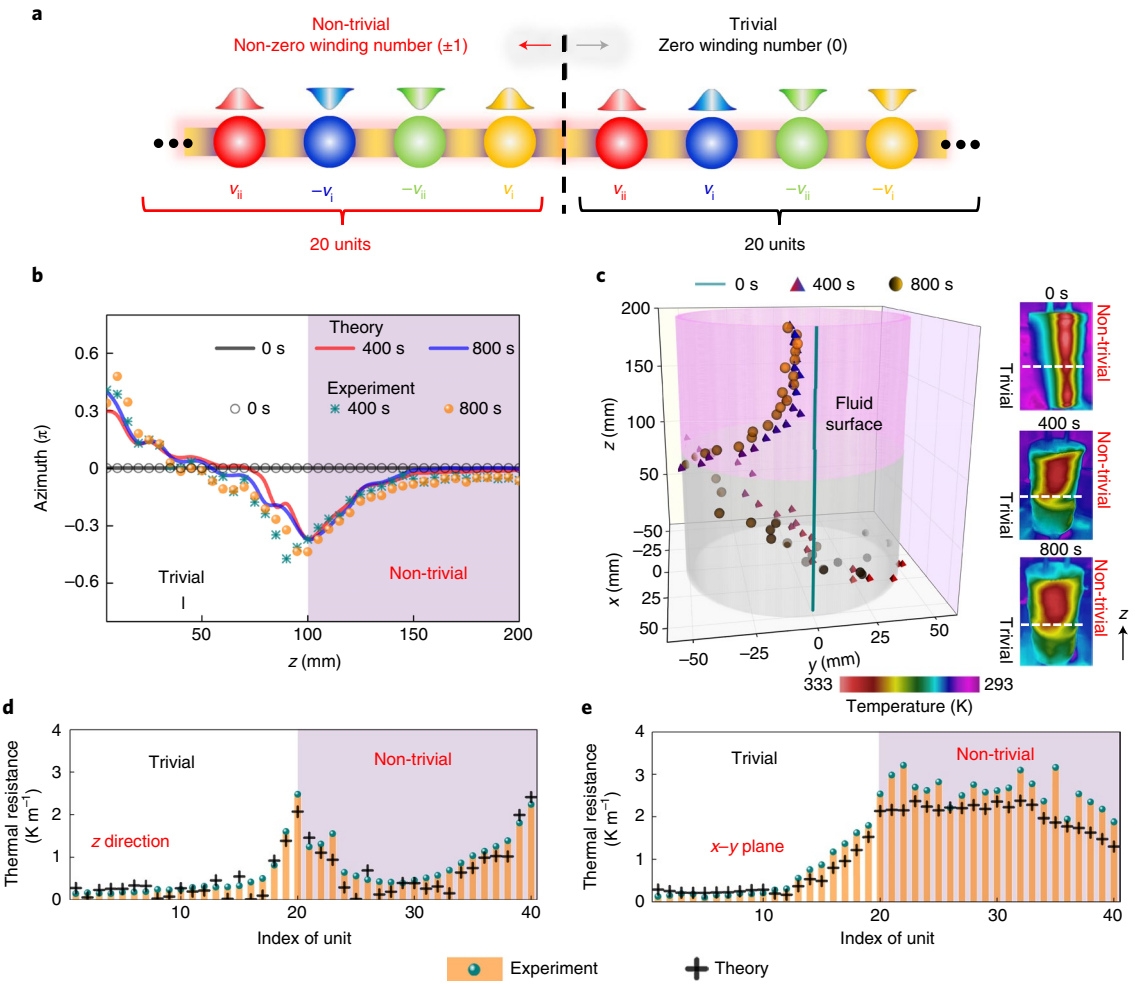


**Fig. 3 | Measured temperature profiles and effective thermal resistances for Case I. a**, Advective configurations of Case I, consisting of five non-trivial (20 units) and five trivial (20 units) lattices. All the advections are selected in Phase III (Supplementary Note 2). **b**, Azimuths of $T_{max}$ for each unit at specific moments. **c**, Visualizations of experimental $T_{max}$ locations on the fluid surface (left) and captured temperature profiles (right). The colour bars in **c** and **d** indicate the temperature ranges of the IR images. The data in **b** and **c** show that the characteristic distributions of non-trivial lattices remain almost stationary, whereas those of trivial lattices move with time and exhibit largely deviated profiles. **d**,**e**, Effective thermal resistances of Case I along the *z* direction (**d**) and in the *x*–*y* plane (**e**). An interface state can be revealed at the joint between the non-trivial and trivial lattices, whereas an edge state is also significant at the boundary between the non-trivial lattice and open ambience. The light-purple shadows in **b**–**d** indicate the regions of non-trivial lattices. In **d** and **e**, the orange columns with green dots denote the experimental values and '+' denotes the theoretical values of the effective thermal resistances of each unit.

The temperature profiles and spatial information of $T_{max}$ (Fig. 2b,d) indicate that the thermal distributions exhibit distinctive differences between the initial and final moments. The characteristic thermal distributions showcase significant deviations towards both sides with respect to their initial positions in the units near both system boundaries and reveal relatively stable distributions in the intermediate units of the system over time. Such behaviours are robustly maintained till the steady state. By further evaluating the state intensities (effective thermal resistances along the *z* direction and *x*–*y* plane) of each unit for the trivial lattices, there are no significant differences between the effective thermal resistances of each unit in these directions, revealing the bulk state on the fluidic surface with zero winding number (Supplementary Note 2). Except the different characteristics of the temperature distributions, the thermal process of the scheme with trivial lattices is enhanced compared with the non-trivial one, since the temperature amplitudes shown in Fig. 2d indicate a faster relaxation process than those shown in Fig. 2c.

The topological edge and bulk states suggest the possibility of flexibly manipulating the thermal properties of a fluidic surface. Here we further explore two cases with the tunable butting of topologically non-trivial and trivial lattices, possessing non-zero (±1) and zero winding numbers, respectively, demonstrating controllable edge, interface and bulk states, whereas the advections are also modulated in the same gapped phase (Supplementary Note 2). For Case I, we configure five non-trivial (20 units) and five trivial (20 units) lattices to the fluidic surface (Fig. 3a). The characteristic thermal distributions and experimental temperature profiles are illustrated in Fig. 3b–e. The spatial information of $T_{max}$ at specific moments (Fig. 3b,c) indicate that the characteristic distributions of non-trivial lattices could maintain stationary locations in most of the units, whereas some deviations to the initial states occur in the units approaching the boundary of non-trivial and trivial lattices. For trivial lattices, the characteristic distributions showcase large deviations to the initial states in most of the intermediary units, whereas the $T_{max}$ locations of the last few units approaching the system boundary further indicate near-π deviations. Such distributions in the non-trivial and trivial lattices reveal one edge state and one interface state at the system boundary in the non-trivial lattice and butting of the two

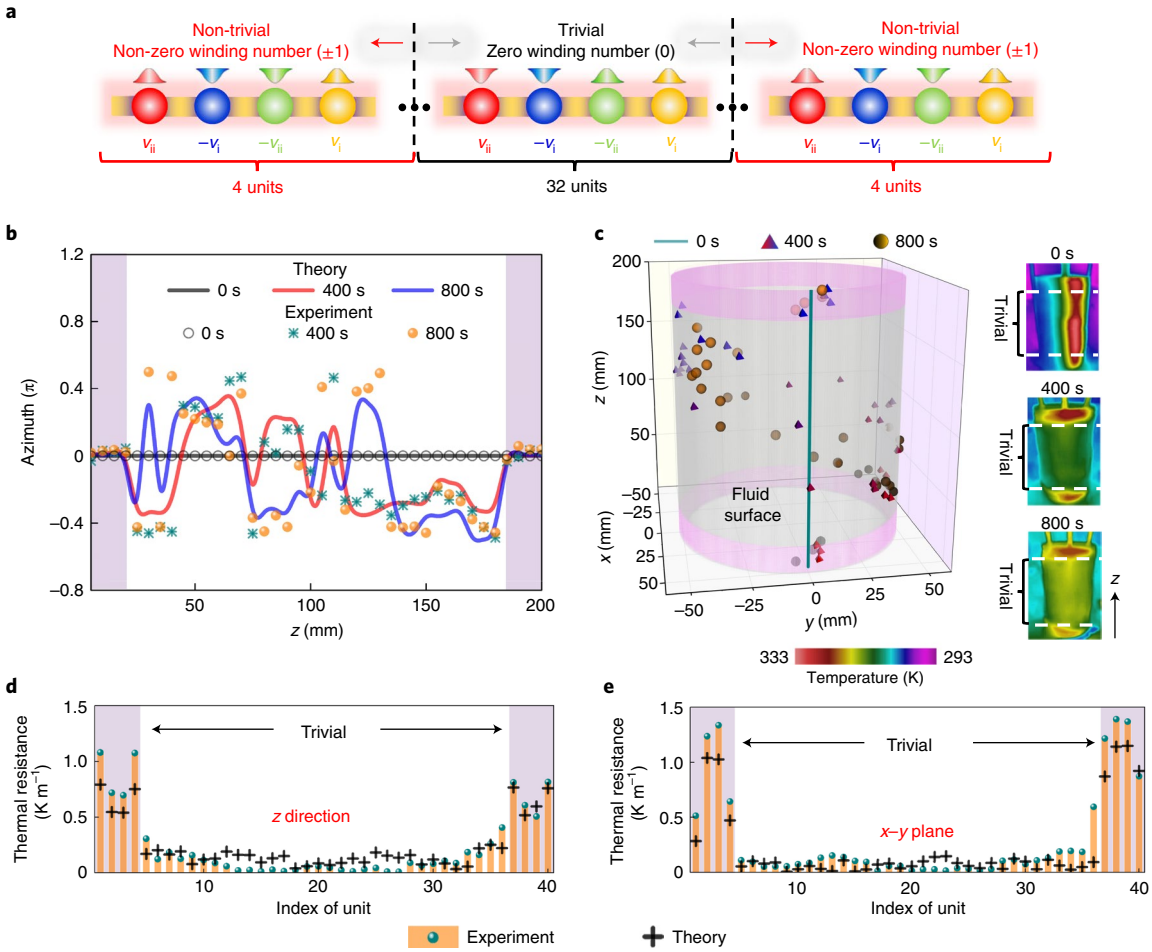


**Fig. 4 | Measured temperature profiles and effective thermal resistances for Case II. a**, Advective configurations of Case II, consisting of two non-trivial lattices (4 units each) on both sides of the entire model and eight trivial lattices (32 units) between the non-trivial ones. All the advections are selected in Phase III. **b**, Azimuths of $T_{max}$ for each unit at specific moments. **c**, Experimental $T_{max}$ locations on the fluid surface (left) and the captured temperature profiles of Case II (right). The colour bars in **c** and **d** indicate the temperature ranges of the IR images. In **b** and **c**, stationary thermal distributions are significant in the two non-trivial lattices at the system boundaries, whereas largely deviated profiles are observed in the remaining trivial lattices. **d**,**e**, Effective thermal resistances of Case II along the *z* direction (**d**) and in the *x*–*y* plane (**e**). Two edge states and two interface states are observed at both boundaries of the entire system and the two joints between the non-trivial and trivial lattices, respectively. The light-purple shadows in **b**–**d** indicate the regions of non-trivial lattices. In **d** and **e**, the orange columns with green dots denote the experimental values and '+' denotes the theoretical values of the effective thermal resistances of each unit.

lattices, respectively, implying larger effective thermal resistance (Fig. 3d,e). The captured temperature profiles (Fig. 3b, right) further validate the above characteristic $T_{max}$ locations and demonstrate the distinctive thermal distributions of the two lattices. Besides, faster relaxation can also be observed in trivial lattices with significant homogenized temperature amplitudes at different moments.

For Case II, we adjust the configuration strategy by inserting one non-trivial lattice (4 units) at the two system boundaries, whereas eight trivial lattices (32 units) are further filled in the regions between the two non-trivial lattices (Fig. 4a). The characteristic distributions of each unit (Fig. 4b,c) indicate that the spatial information of $T_{max}$ of the two non-trivial lattices at the system boundaries remain almost unchanged during the measured thermal processes, whereas those of the trivial lattices exhibit significant deviations from the initial states. The experimental temperature profiles at specific moments (Fig. 4c, right) further manifest the thermal behaviour in these lattices, revealing almost stationary profiles in the two non-trivial lattices and largely deviated distributions in the trivial lattices. Besides, faster relaxations can also be indicated in the trivial lattices with quicker temperature homogenizations than the non-trivial ones. By further evaluating the state intensities with the effective thermal resistance (Fig. 4d,e), two edge states at both system boundaries and two interface states at the butting of the non-trivial and trivial lattices are observed with larger (smaller) effective thermal resistances along the *z* direction (in the *x*–*y* plane) compared with the units of trivial lattices. The above two cases reveal the possibility of flexibly manipulating the thermal properties on a fluidic surface with non-trivial and trivial lattices, and more modulations can be anticipated with different lattice configurations and advections.

This work introduces an advective route to reveal the thermal topological modes by stacking periodic advections on a fluid surface. These spatiotemporally modulated advections introduce manipulation in momentum space for a purely dissipative phenomenon like thermal diffusion, enabling effectively non-trivial and trivial lattices. Thermal topological edge, interface and bulk states were observed on modulating the advections within these effective lattices in a gapped phase. Our findings point to a direction beyond conventional topological physics based on oscillatory fields,

offering a unique platform to study unexpected non-Hermitian topological modes in purely diffusive systems. The critical strategy is to create the conduction–advection form in different diffusive fields with actual or effective advective terms. If the actual advection does not naturally exist such as electric conductivity, one feasible way is to adopt spatiotemporal parameters to derive an effective advective term from the intrinsic conduction. Besides, this work also suggests a distinctive mechanism of arbitrary diffusive manipulations with combinations of non-trivial and trivial lattices.

## Online content

Any methods, additional references, Nature Research reporting summaries, source data, extended data, supplementary information, acknowledgements, peer review information; details of author contributions and competing interests; and statements of data and code availability are available at https://doi.org/10.1038/s41567-021-01493-9.

Received: 19 August 2021; Accepted: 10 December 2021;
Published online: 03 February 2022

## References

1. Yang, Y. et al. Realization of a three-dimensional photonic topological insulator. *Nature* **565**, 622–626 (2019).
2. Lustig, E. et al. Photonic topological insulator in synthetic dimensions. *Nature* **567**, 356–360 (2019).
3. Zilberberg, O. et al. Photonic topological boundary pumping as a probe of 4D quantum Hall physics. *Nature* **553**, 59–62 (2018).
4. Liu, Y. et al. Bulk–disclination correspondence in topological crystalline insulators. *Nature* **589**, 381–385 (2021).
5. Stützer, S. et al. Photonic topological Anderson insulators. *Nature* **560**, 461–465 (2018).
6. Shen, H., Zhen, B. & Fu, L. Topological band theory for non-Hermitian Hamiltonians. *Phys. Rev. Lett.* **120**, 146402 (2018).
7. Ghatak, A. & Das, T. New topological invariants in non-Hermitian systems. *J. Phys.: Condens. Matter* **31**, 263001 (2019).
8. Feng, L., El-Ganainy, R. & Ge, L. Non-Hermitian photonics based on parity–time symmetry. *Nat. Photon.* **11**, 752–762 (2017).
9. Wang, K. et al. Generating arbitrary topological windings of a non-Hermitian band. *Science* **371**, 1240–1245 (2021).
10. Khanikaev, A. B. et al. Photonic topological insulators. *Nat. Mater.* **12**, 233–239 (2013).
11. Chen, Z. & Segev, M. Highlighting photonics: looking into the next decade. *eLight* **1**, 2 (2021).
12. Hokmabadi, M. P., Schumer, A., Christodoulides, D. N. & Khajavikhan, M. Non-Hermitian ring laser gyroscopes with enhanced Sagnac sensitivity. *Nature* **576**, 70–74 (2019).
13. Hadad, Y., Soric, J. C., Khanikaev, A. B. & Alu, A. Self-induced topological protection in nonlinear circuit arrays. *Nat. Electron.* **1**, 178–182 (2018).
14. Leykam, D., Bliokh, K. Y., Huang, C., Chong, Y. D. & Nori, F. Edge modes, degeneracies, and topological numbers in non-Hermitian systems. *Phys. Rev. Lett.* **118**, 040401 (2017).
15. Xu, H., Mason, D., Jiang, L. & Harris, J. G. E. Topological energy transfer in an optomechanical system with exceptional points. *Nature* **537**, 80–83 (2016).
16. Doppler, J. et al. Dynamically encircling an exceptional point for asymmetric mode switching. *Nature* **537**, 76–79 (2016).
17. Lin, Z. et al. Unidirectional invisibility induced by $\mathcal{PT}$-symmetric periodic structures. *Phys. Rev. Lett.* **106**, 213901 (2011).
18. Peng, B. et al. Parity-time-symmetric whispering-gallery microcavities. *Nat. Phys.* **10**, 394–398 (2014).
19. Peng, B. et al. Loss-induced suppression and revival of lasing. *Science* **346**, 328–332 (2014).
20. Zhao, H. et al. Topological hybrid silicon microlasers. *Nat. Commun.* **9**, 981 (2018).
21. Zhao, H. et al. Non-Hermitian topological light steering. *Science* **365**, 1163–1166 (2019).
22. Zeng, Y. et al. Electrically pumped topological laser with valley edge modes. *Nature* **578**, 246–250 (2020).
23. Bandres, M. A. et al. Topological insulator laser: experiments. *Science* **359**, eaar4005 (2018).
24. Harari, G. et al. Topological insulator laser: theory. *Science* **359**, eaar4003 (2018).
25. Choi, J. H. et al. Room temperature electrically pumped topological insulator lasers. *Nat. Commun.* **12**, 3434 (2021).
26. Bahari, B. et al. Nonreciprocal lasing in topological cavities of arbitrary geometries. *Science* **358**, 636–640 (2017).
27. Liang, G. Q. & Chong, Y. D. Optical resonator analog of a two-dimensional topological insulator. *Phys. Rev. Lett.* **110**, 203904 (2013).
28. Takata, K. & Notomi, M. Photonic topological insulating phase induced solely by gain and loss. *Phys. Rev. Lett.* **121**, 213902 (2018).
29. Li, M., Ni, X., Weiner, M., Alù, A. & Khanikaev, A. B. Topological phases and nonreciprocal edge states in non-Hermitian Floquet insulators. *Phys. Rev. B* **100**, 45423 (2019).
30. Liertzer, M. et al. Pump-induced exceptional points in lasers. *Phys. Rev. Lett.* **108**, 173901 (2012).
31. Feng, L., Wong, Z. J., Ma, R. M., Wang, Y. & Zhang, X. Single-mode laser by parity-time symmetry breaking. *Science* **346**, 972–975 (2014).
32. Yoon, J. W. et al. Time-asymmetric loop around an exceptional point over the full optical communications band. *Nature* **562**, 86–90 (2018).
33. Xia, S. et al. Nontrivial coupling of light into a defect: the interplay of nonlinearity and topology. *Light Sci. Appl.* **9**, 147 (2020).
34. Xia, S. et al. Nonlinear tuning of PT symmetry and non-Hermitian topological states. *Science* **372**, 72–76 (2021).
35. Liu, S. et al. Gain- and loss-induced topological insulating phase in a non-Hermitian electrical circuit. *Phys. Rev. Appl.* **13**, 014047 (2020).
36. Gao, H. et al. Non-Hermitian route to higher-order topology in an acoustic crystal. *Nat. Commun.* **12**, 1888 (2021).
37. Li, Y. et al. Anti–parity-time symmetry in diffusive systems. *Science* **364**, 170–173 (2019).
38. Fan, C. Z., Gao, Y. & Huang, J. P. Shaped graded materials with an apparent negative thermal conductivity. *Appl. Phys. Lett.* **92**, 251907 (2008).
39. Han, T. et al. Experimental demonstration of a bilayer thermal cloak. *Phys. Rev. Lett.* **112**, 054302 (2014).
40. Zhou, X., Xu, G. & Zhang, H. Y. Binary masses manipulation with composite bilayer metamaterial. *Compos. Struct.* **267**, 113866 (2021).
41. Zhou, X. & Xu, G. Self-adaptive field manipulation with thermal logic material. *Int. J. Heat Mass Trans.* **172**, 121147 (2021).
42. Xu, G. et al. Tunable analog thermal material. *Nat. Commun.* **11**, 6028 (2020).
43. Torrent, D., Poncelet, O. & Batsale, J.-C. Nonreciprocal thermal material by spatiotemporal modulation. *Phys. Rev. Lett.* **120**, 125501 (2018).

## Methods

**Transition between schematic and actual models.** The schematic of a planar fluid surface in virtual space $(x_p, y_p, z)$ and the practical annular fluid surface in transformed space $(x, y, z)$ are shown in Fig. 1a,c. To mimic the oscillations and periodic propagations in thermal diffusion, we make the advections transfer along the $x_p$ direction in the virtual space of the model. However, it brings great challenges in practical implementations for a finite thermal system. Here we connect the two terminals along the $x_p$ direction in the virtual space, thus forming an annular fluid surface in the transformed space to create the effective model for practical experiments. Such a transition can be regarded as a general conformal mapping from the virtual space $(x_p, y_p, z)$ to the transformed space $(x, y, z)$ under the relation $e^{y_p+ix_p}$ around the $z$ direction (direction of lattice arrangement). In that case, the $z$ directions shown in Fig. 1a,c are consistent. The $x_p$ direction (parallel to the imaginary axis) shown in Fig. 1a becomes the azimuthal direction around the perimeter of the annular fluid surface (Fig. 1c). The $y_p$ direction (parallel to the real axis; Fig. 1a) transforms into the radial direction (Fig. 1c), satisfying $R = e^{y_p}$. After the above transformation, the imposed advections (Fig. 1c) now propagate along the perimeter of the annular fluid surface around the $z$ direction, whereas the oscillatory properties in Fig. 1a (along the $x_p$ direction) can remain the same in the effective model (Fig. 1c). It is worth noting that the Cartesian system, instead of a cylindrical one, is adopted as the general coordinate in the transformed space (Fig. 1c) for easy data collection in practical implementations, since the direct measured data captured by dynamic components and thermocouples are in the form of Cartesian coordinates.

**Experimental structure and actuation of the measured sample.** After the theoretical spatial transition, an annular fluid surface with radius $R$ (Fig. 1c) is created in the transformed space $(x, y, z)$. This surface is the objective for realizing the effective lattice in thermal diffusion and observing the underlying topological transitions. To simultaneously modulate the different lattice units on this fluid surface, we insert four independent gear sets (including one internal gear and one driving gear) on each lattice type to impose tailored advections on the specific units via four transmission shafts (Fig. 1c and Extended Data Fig. 1; same colours are adopted to mark the correspondence between the gear sets and specific fluid regions/units). Considering the lattice periodicity along the $z$ direction and lattice constant $4a$, we only need to keep the same advection on the congeneric units of the other lattices (marked using the same colours). Hence, we configure multiple driving gears on each transmission shaft with the interval of $4a$ (lattice constant) between two neighbours and then combine the four types of gear set, thus forming the real structure shown in Fig. 1c and Extended Data Fig. 1. In that case, each congeneric unit on the fluid surface coated outside the internal gears can be simultaneously modulated by tailored functions via the same transmission shaft. Note that all these gear sets as well as specific units should implement concentric rotations to observe the continuous temperature fields on the annular fluid surface. Hence, we further set a constraint outside the entire structure to guarantee concentric rotations (Extended Data Fig. 1). For the experimental measurements at specific moments, the constraint is removed to directly observe the temperature distributions of the fluid surface. Additional visualizations can be found in Supplementary Videos 1–5.

**Fabricated parameters and general setups.** The schematic and fabricated samples are illustrated in Extended Data Fig. 1. The advections on the annular fluid surface are imposed by the corresponding advective components, that is, the gear sets including one internal gear and one driving gear for each. All these advective components are made of polycaprolactam with a thermal conductivity of $1.2\,W\,m^{-1}\,K^{-1}$. The external and internal radii of the spinning rings are $R_{ext} = 50.0$ mm and $R_{int} = 47.5$ mm, respectively; further, 40 inner teeth are inlaid into the internal surface of the spinning rings and the thickness of each spinning ring is 5 mm. Each driving gear is equipped with 20 teeth, whose external radius and thickness are 34 and 5 mm, respectively. Four transmission shafts made of polycaprolactam are employed to hold the driving gears for implementing the required advections of the non-trivial and trivial lattices. Here 10 driving gears are installed on each transmission shaft with an interval of 20 mm between the central points of two neighbours, and spatiotemporal excitations corresponding to each unit within the lattice are imposed on the transmission shafts. The transmission ratio of the gear system is 2; thus, double velocities than the internal gears should be imposed on the driving gears. A constraint shell made of polyamide 66 (PA66) with a conductivity of $0.24\,W\,m^{-1}\,K^{-1}$, thickness of 0.5 mm, length of 30.0 mm and internal radius of 51.0 mm is fabricated to concentrically hold the advective components. The interspace between the shell and advective components is filled with grease ($1.2\,W\,m^{-1}\,K^{-1}$; $d = 1$ mm) to act as the fluidic surface for supporting the thermal topological behaviours. Thus, the advective components could be located at the downward side of the fluid surface and provide momentums on the fluid surface. The initial temperature profile is provided by a heating strip on one side of the outermost shell, whereas a constant-temperature (room temperature) strip is attached to the opposite side of the heating one during the heating process. After heating for 30 min, the sources are removed, and the motors are started. All the temperature profiles are captured by an infrared (IR) camera with a setting emissivity of 0.97.

**Experimental demonstrations for insulating phases.** The motors are started after the heating process. Based on the fabricated parameters of the system, the critical values on the exceptional points (EPs) should follow $k^2 v_i v_{ii} = (m_{EP})^2 = (\kappa/\rho cbd)^2 = 0.0225\,s^{-2}$. Four independent motors for spinning motions are employed to demonstrate the selected insulating phases and non-trivial/trivial behaviours (Fig. 2). The spatiotemporal advections for the four axes are $2|R_{ext}m_{EP}\sin(2\pi/10t)|$, $-|R_{ext}m_{EP}\sin(2\pi/10t)|$, $-2|R_{ext}m_{EP}\sin(2\pi/10t)|$ and $|R_{ext}m_{EP}\sin(2\pi/10t)|$, where $t$ denotes time. The spatial information of $T_{max}$ is measured by a thermocouple and dynamic components, whose data format is in the form of Cartesian coordinates. Thus, the experimental $T_{max}$ azimuths (Figs. 2–4) can be calculated as $\theta = \arctan\left(\frac{y}{x}\right)$.

**Experimental systems for topological manipulations.** Since the demonstrations of manipulated Cases I and II require different lattice configurations on the fluidic surface under corresponding advections, additional transmission shafts and motors are employed to implement the experiments. For Case I, the fluid surface is actuated by five non-trivial (20 units) and five trivial (20 units) lattices. The velocities of the non-trivial/trivial components are independently modulated by four transmission shafts corresponding to the four advective configurations of each lattice. The spinning velocities for each unit of one non-trivial lattice are $3|R_{ext}m_{EP}\sin(2\pi/10t)|$, $-2|R_{ext}m_{EP}\sin(2\pi/10t)|$, $-3|R_{ext}m_{EP}\sin(2\pi/10t)|$ and $2|R_{ext}m_{EP}\sin(2\pi/10t)|$, whereas the velocities for each unit of the trivial lattice are $3|R_{ext}m_{EP}\sin(2\pi/10t)|$, $2|R_{ext}m_{EP}\sin(2\pi/10t)|$, $-3|R_{ext}m_{EP}\sin(2\pi/10t)|$ and $-2|R_{ext}m_{EP}\sin(2\pi/10t)|$. The same modulated method is also implemented in Case II. Considering the advective configurations and manipulated behaviours, two non-trivial lattices (4 units each) at both system boundaries and eight trivial lattices (32 units) between them are adopted. The advective velocities for each of the 4 units in the non-trivial lattices are $3|R_{ext}m_{EP}\sin(2\pi/10t)|$, $-2|R_{ext}m_{EP}\sin(2\pi/10t)|$, $-3|R_{ext}m_{EP}\sin(2\pi/10t)|$ and $2|R_{ext}m_{EP}\sin(2\pi/10t)|$, whereas the velocities for each unit of the internal trivial lattice are $3|R_{ext}m_{EP}\sin(2\pi/10t)|$, $2|R_{ext}m_{EP}\sin(2\pi/10t)|$, $-2|R_{ext}m_{EP}\sin(2\pi/10t)|$ and $-3|R_{ext}m_{EP}\sin(2\pi/10t)|$.

## Data availability

Source data are provided with this paper. All other data that support the plots within this paper and other findings of this study are available from the corresponding author upon reasonable request.

## Acknowledgements

C.-W.Q. acknowledges financial support from the Ministry of Education, Republic of Singapore (grant no. R-263-000-E19-114). A.A. acknowledges financial support from the Office of Naval Research with grant no. N00014-19-1-2011, the Vannevar Bush Faculty Fellowship, the Air Force Office of Scientific Research with MURI grant no. FA9550-18-1-0379 and the Simons Foundation. Y.Y. and H.C. acknowledge the National Natural Science Foundation of China (NNSFC) under grant nos. 61625502, 61975176, 11961141010 and 62175215; the Top-Notch Young Talents Program of China; and the Fundamental Research Funds for the Central Universities. X.Z. acknowledges financial support from the Chongqing Natural Science Foundation (grant no. cstc2021jcyj-msxmX0627) and the Science and Technology Research Program of Chongqing Municipal Education Commission (grant no. KJQN202000829).

## Author contributions

G.X. and C.-W.Q. conceived the idea. G.X., X.Z. and C.-W.Q. proposed the methodology. G.X., Y.Y., H.C., A.A. and C.-W.Q. performed the theoretical derivations. G.X. and X.Z. implemented the experimental investigations. G.X., Y.Y., X.Z. and C.-W.Q. made the visualizations. G.X., Y.Y., H.C., A.A. and C.-W.Q. performed the theoretical analysis and wrote the manuscript. C.-W.Q. supervised the work. All the authors contributed to the discussion and to finalizing the manuscript.

## Competing interests

The authors declare no competing interests.

## Additional information

**Extended data** is available for this paper at https://doi.org/10.1038/s41567-021-01493-9.

**Supplementary information** The online version contains supplementary material available at https://doi.org/10.1038/s41567-021-01493-9.

**Correspondence and requests for materials** should be addressed to Cheng-Wei Qiu.

**Peer review information** *Nature Physics* thanks Muamer Kadic and the other, anonymous, reviewer(s) for their contribution to the peer review of this work.

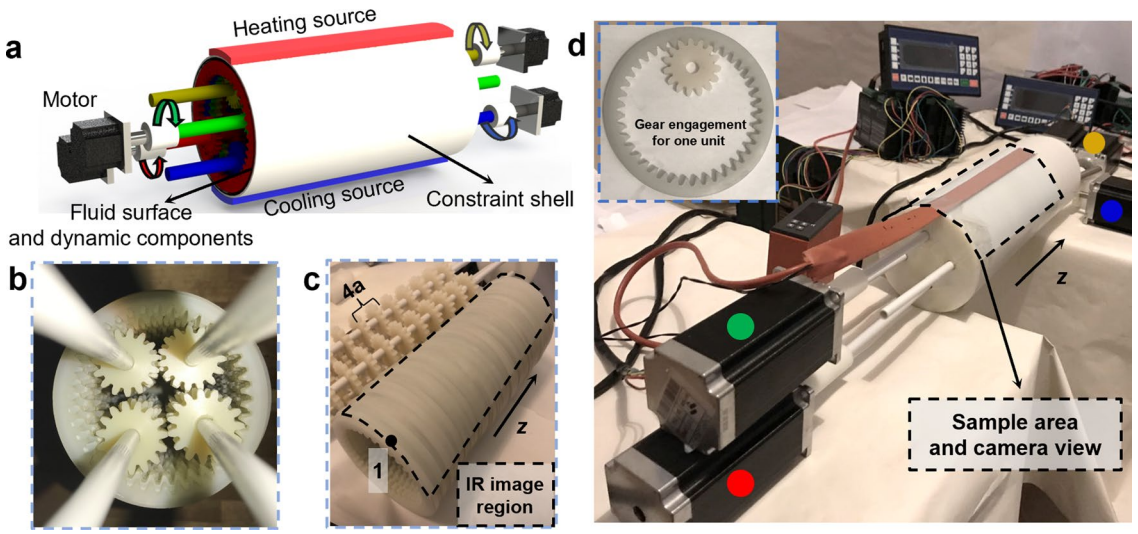


**Extended Data Fig. 1 | The entire structure and experimental setups. a** indicates the entire structure for implementing advections (effective oscillations) on the fluid surface, a constraint shell is adopted outside the fluid surface to keep the concentric rotations for each unit and the internal gear. During the measurements, this constraint shell is removed to directly capture the temperature-related data of the fluid surface. **b** and **c** present the fabricated dynamic components and their combinations consisting of 40 internal gear sets for modulating the fluid surface. The azimuthal direction of the units is marked in (**b**). The black dashed border in (**c**) indicates the region for IR images when fluid is coated on these dynamic components, while the interval of two neighboring deriving gears on a transmission shaft is 4a. The black dot marked with '1' indicates the first unit of the entire system at the initial location of $z = 0$. **d** provides the real experiment setups, and the left upper inset presents the general engagement of the internal gear set for one unit cell. The colored dots indicate the corresponding motors.